magnetochemistry

MDPI

Article

Diverse Magnetic Properties of Two New Binuclear Complexes Affected by [FeN_6] Octahedral Distortion: Two-Step Spin Crossover versus Antiferromagnetic Interactions

Yue Gao [1,†], Yu-Qin Li [1,†], Yao Li [1], Jing-Wei Dai [2,*], Jin-Hua Wang [3], Ying-Ying Wu [1], Masahiro Yamashita [4] and Zhao-Yang Li [1]

[1] School of Materials Science and Engineering, Nankai University, 38 Tongyan Road, Tianjin 300350, China
[2] State Key Laboratory of Medicinal Chemical Biology, Nankai University, 94 Weijin Road, Tianjin 300071, China
[3] College of Medicine and Nursing, Dezhou University, Dezhou 253023, China
[4] Department of Chemistry, Graduate School of Science, Tohoku University, 6-3 Aramaki-Aza-Aoba, Aoba-Ku, Sendai 980-8578, Japan
* Correspondence: jingweidai@nankai.edu.cn
† These authors contributed equally to this work.

Abstract: Polymetallic complexes with covalently bridged metal centers that interact magnetically are important in the molecular magnetism field, with binuclear compounds receiving special attention because they represent the simplest type of multinuclear species with covalently bridged metal centers. Herein, we report the synthesis and properties of two new binuclear Fe^{II} complexes, namely, {[Fe(abpt-TPE)$(NCS)_2$]$_2$(bpym)}·2MeOH·2MeCN (**1**) and {[Fe(abpt-TPE)$(NCS)_2$]$_2$(bpym)}·2CH_2Cl_2 (**2**) (bpym = 2,2′-bipyrimidine). The crystal structure is analyzed at different temperatures, and its properties are analyzed by variable-temperature magnetic susceptibility and variable-temperature fluorescence emission spectroscopy tests. Variable-temperature magnetic susceptibility measurements of two binuclear compounds show different types of magnetic behavior. Complex **1** exhibits two-step spin transition behavior with an intermediate state near 150 K (T_{c1} = 191 K, T_{c2} = 111 K); **1** undergoes an [LS–LS] ↔ [LS–HS] ↔ [HS–HS] spin transition during thermal induction. On the other hand, complex **2** exhibits intramolecular antiferromagnetic coupling, with $J = -0.47$ cm^{-1}. The analysis of correlations between the structural characteristics and different types of magnetic behaviors for two binuclear complexes, revealed that the different magnetic behaviors shown by the two complexes are attributable to different degrees of [FeN_6] octahedral distortion caused by different lattice solvents, ligand strain and crystal stacking.

Keywords: magnetic bistability; spin crossover; antiferromagnetic interactions; two-step spin transition; supramolecular structures

Citation: Gao, Y.; Li, Y.-Q.; Li, Y.; Dai, J.-W.; Wang, J.-H.; Wu, Y.-Y.; Yamashita, M.; Li, Z.-Y. Diverse Magnetic Properties of Two New Binuclear Complexes Affected by [FeN_6] Octahedral Distortion: Two-Step Spin Crossover versus Antiferromagnetic Interactions. *Magnetochemistry* **2023**, *9*, 69. https://doi.org/10.3390/magnetochemistry9030069

Academic Editor: Carlos J. Gómez García

Received: 14 February 2023
Revised: 24 February 2023
Accepted: 25 February 2023
Published: 28 February 2023

1. Introduction

Designing and developing molecular switches capable of storing or transmitting information are among the most attractive research endeavors [1–6]. As typical bistable magnetic materials, spin crossover (SCO) complexes exhibit bistable high-spin (HS) and low-spin (LS) characteristics that interconvert when exposed to external stimuli, such as temperature, light and pressure; hence, SCO materials are ideal molecular systems for realizing magnetic switches and information storage elements. Cooperativity caused by crystal stacking interactions or size/shape differences between the HS and LS states is a crucial characteristic of SCO, which may significantly impact the SCO properties of solid complexes [7–9]. Compared with mononuclear systems, which are currently the most researched SCO systems [10–12], bridging SCO centers through covalent bonds represents an important way of exploring and enhancing system cooperativity [13–19]. Moreover, covalently bridged metal centers can effectively couple magnetically [20–23].

Designing and synthesizing multinuclear systems, which includes effectively controlling the number of nuclear centers as well as crystal characterization techniques, is still somewhat challenging [24]. Exploring binuclear systems is a valuable endeavor because they are the simplest and smallest systems in which two metal centers interact and in which intramolecular and intermolecular cooperativity can be investigated [25]. The first binuclear Fe^{II} SCO complex was synthesized by bridging a ligand with μ-bipyrimidine (bpym).

In this study, we used an *N*-(3,5-di(pyridine-2-yl)-4*H*-1,2,4-triazol-4-yl)-1-(4-(1,2,2-triphenylvinyl)phenyl)methanimine (abpt-TPE) [26,27] fluorescent ligand as the terminal ligand and bpym (with a suitable medium field strength) as the bridging ligand [28–34]. By adjusting the synthetic scheme, we prepared two new binuclear complexes, namely, {[Fe(abpt-TPE)$(NCS)_2$]$_2$(bpym)}·2MeOH·2MeCN (**1**) and {[Fe(abpt-TPE)$(NCS)_2$]$_2$(bpym)}·$2CH_2Cl_2$ (**2**). Complex **1** exhibited two-step spin transition behavior, whereas complex **2** remained in the HS state throughout the examined temperature range, with intramolecular antiferromagnetic Fe^{II}_{HS} coupling observed ($J = -0.47$ cm^{-1}). In addition, we speculate that the different magnetic behaviors exhibited by the two complexes are due to differences in [FeN_6] octahedral distortion. We studied the fluorescence properties of **1** using variable-temperature fluorescence spectroscopy, which revealed that complex **1** exhibits concurrent fluorescence and SCO behavior. Herein, we aim to contribute to the design and synthesis of binuclear and multinuclear magnetic complexes.

2. Results and Discussion

The acquired powder X-ray diffraction (PXRD) data for complexes **1** and **2** were compared with simulated data (Figure S1), with consistent sets of spectra obtained, confirming that **1** and **2** are pure. Complexes **1** and **2** were subjected to thermal gravimetric analysis (TGA) to examine their thermal stabilities (Figure S2). The TGA traces of both complexes reveal that solvent molecules are gradually lost with increasing temperature.

Crystalline samples of complex **1** were subjected to magnetic susceptibility experiments in the 5–300 K temperature range in a 1000 Oe external magnetic field. Figure 1a shows that complex **1** exhibits gradual two-step spin crossover behavior, for which the spin transition temperature is T_{c1} = 191 K and T_{c2} = 111 K. A $\chi_M T$ value of 7.25 cm^3 K mol^{-1} was observed at 300 K, which corresponds to Fe^{II}_{HS}; $\chi_M T$ was observed to continuously decrease with decreasing temperature to an intermediate state at 150 K with a $\chi_M T$ value of 3.79 cm^3 K mol^{-1}, which corresponds to the first SCO step. The $\chi_M T$ value decreased to 0.68 cm^3 K mol^{-1} as the temperature was further decreased to 10 K, consistent with the second SCO step. The HS and LS states of Fe^{II} account for approximately 50% each at 150 K. Measurements in heating and cooling modes revealed identical thermal hysteresis-free magnetic behavior, which was reproducible in consecutive cycles.

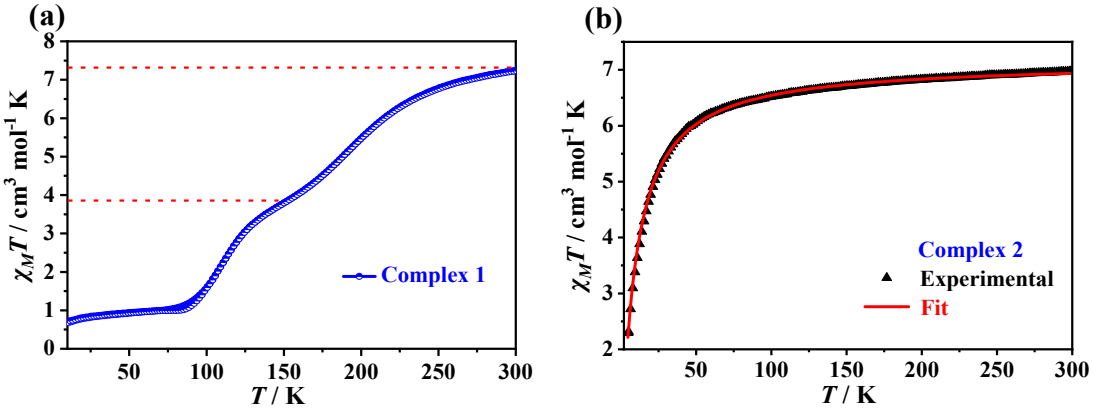

Figure 1. Magnetic susceptibilities ($\chi_M T$) of (**a**) {[Fe(abpt-TPE)$(NCS)_2$]$_2$(bpym)}·2MeOH·2MeCN (**1**) and (**b**) {[Fe(abpt-TPE)$(NCS)_2$]$_2$(bpym)}·$2CH_2Cl_2$ (**2**) as functions of *T*. The solid red line shows the line of best fit obtained using the *PHI* program.

The magnetic susceptibility of **2** was measured under the abovementioned conditions. Figure 1b shows that complex **2** exhibited a $\chi_M T$ value of 6.97 cm^3 K mol^{-1} at 300 K, which decreased at first with decreasing temperature and then rapidly from 50 K to a value of 2.29 cm^3 K mol^{-1} at 5 K. The observed change in $\chi_M T$ with temperature reveals the presence of antiferromagnetic coupling between intramolecular [HS–HS] pairs in complex **2** [35]. We fitted the experimental magnetic susceptibility data using the PHI program to further examine the intramolecular antiferromagnetic $Fe^{II}{}_{HS}$ coupling, as described by Wang et al. [22], the results of which are shown in Figure 1b, which yielded $J = -0.47$ cm^{-1} and $g = 2.18$. The negative J value further confirms the existence of antiferromagnetic coupling between intramolecular [HS–HS] pairs.

We also acquired the magnetization (M–H) curve for complex **2** in the 0–7 T range (Figure S3). The magnetization of **2** increased linearly with increasing magnetic field in the 0–4 T range; however, the slope of the M–H curve increased in the 4–7 T range. Complex **2** exhibited a maximum magnetization of 3.6 μB at 7 T, which is lower than its theoretical value of 4 μB. These values are consistent with the antiferromagnetic interaction generated by the [HS–HS] state in **2**.

Differential scanning calorimetry (DSC) at 5 K min^{-1} was used to further explore the thermally induced spin crossover behavior of complex **1**. Figure S4 shows broad exothermic and endothermic peaks at 186 and 193 K, respectively, with ΔH values of approximately 2.89 and 2.71 kJ mol^{-1} and ΔS values of approximately 15.53 and 14.36 J mol^{-1} K^{-1}, respectively. The temperature range corresponding to the exothermic and endothermic peaks is consistent with the first step in the magnetically measured SCO process. Complex **1** exhibited a second spin crossover temperature $T_{c2} = 111$ K that approached the temperature limit of the DSC instrument, and its peak value was difficult to determine.

Single-crystal structures of complex **1** were collected at 100, 150, and 300 K, while single crystal data were collected at 100 K for **2**. Complexes **1** and **2** crystallize in the triclinic P-1 ($Z = 1$) and monoclinic $P2_1/n$ ($Z = 2$) space groups, respectively (Tables S1 and S2). Figures 2 and 3 show the molecular structures and corresponding atomic numbering systems for **1** and **2** at 100 K, respectively. The two complexes exhibit similar coordination modes: Fe^{II} exists in a distorted N_6 octahedral environment, coordinated by two NCS nitrogen atoms, the bridging bpym ligand, and two nitrogen atoms of the abpt-TPE ligand. **1** and **2** consist of centrally symmetric binuclear units. The midpoint of the bpym ligand connected to the metal center coincides with the inversion center. The smallest asymmetric unit of **1** contains half a molecule, as well as a methanol and acetonitrile molecule, while the asymmetric unit of **2** contains half a molecule and a dichloromethane molecule. Complete structures **1** and **2** were generated using the inversion center.

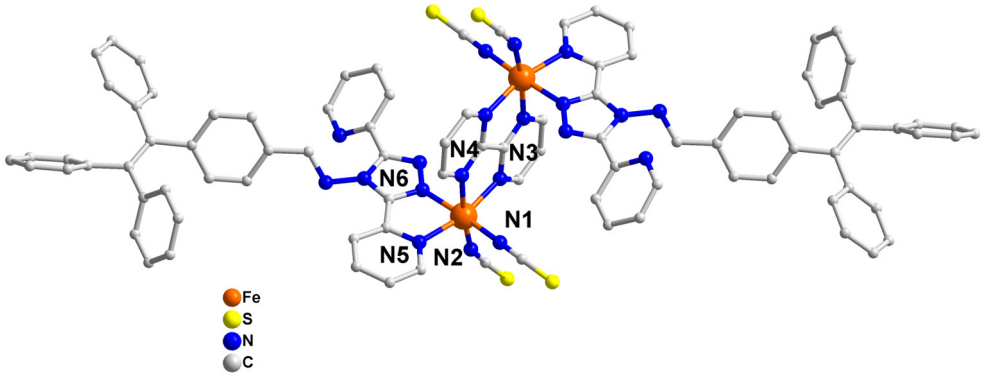

Figure 2. Molecular structure of {[Fe(abpt-TPE)$(NCS)_2]_2$(bpym)}·2MeOH·2MeCN (**1**) at 100 K. Hydrogen atoms and solvent molecules have been omitted for clarity.

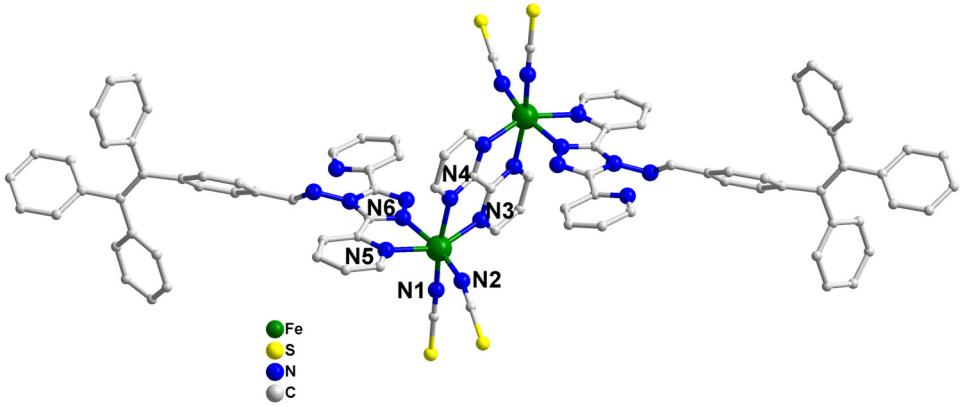

Figure 3. Molecular structure of {[Fe(abpt-TPE)$(NCS)_2]_2$(bpym)}·$2CH_2Cl_2$ (**2**) at 100 K. Hydrogen atoms and solvent molecules have been omitted for clarity.

The Fe(1)–N(1)–C(1) angles in **1** were determined to be 176.7(4)°, 175.8(3)°, and 173.6(7)°, respectively, at 100, 150, and 300 K, leading to nearly linear structures; the corresponding Fe(2)–N(2)–C(2) angles were determined to be 157.9(4)°, 157.4(3)°, and 158.0 (8)°, respectively, at the same temperatures, which deviate significantly from linearity. Complex **2** exhibits an Fe(1)–N(1)–C(1) angle of 168.0(3)°, which significantly deviates from the linearity observed in **1**, while the Fe(2)–N(2)–C(2) angle is 159.3(3)°, which deviates less than the corresponding angle in **1** (Tables 1 and 2).

Table 1. Selected bond lengths [Å] and angles [°] in the structures of complex **1** at various temperatures.

Complex 1	100 K	150 K	300 K
Fe(1)–N(1)	1.967 (4)	1.994 (3)	2.083 (8)
Fe(1)–N(2)	1.933 (5)	1.953 (5)	2.024 (9)
Fe(1)–N(3)	2.059 (3)	2.097 (3)	2.215 (6)
Fe(1)–N(4A)	2.065 (3)	2.115 (3)	2.278 (6)
Fe(1)–N(5)	2.055 (4)	2.088 (3)	2.211 (7)
Fe(1)–N(6)	1.980 (3)	2.019 (3)	2.148 (6)
av. Fe–N(Å)	2.010	2.045	2.161
Σ	51.83	60.37	90.75
$Fe–Fe_{intramolecular}$(Å)	5.544	5.645	5.970
N(1)–Fe(1)–N(2)	92.04 (16)	93.07 (13)	96.8 (3)
N(1)–Fe(1)–N(3)	96.54 (15)	97.77 (12)	101.2 (3)
N(1)–Fe(1)–N(4A)	88.80 (14)	88.48 (12)	87.3 (3)
N(1)–Fe(1)–N(5)	93.85 (15)	93.67 (12)	94.1 (3)
N(1)–Fe(1)–N(6)	171.35 (14)	169.78 (11)	164.5 (3)
N(2)–Fe(1)–N(3)	91.21 (15)	91.99 (12)	92.6 (3)
N(2)–Fe(1)–N(4A)	171.19 (15)	170.40 (12)	166.0 (3)
N(2)–Fe(1)–N(5)	97.75 (15)	98.82 (13)	103.8 (3)
N(2)–Fe(1)–N(6)	93.65 (15)	94.22 (13)	95.9 (3)
N(3)–Fe(1)–N(4A)	79.99 (13)	78.42 (10)	73.5 (2)
N(3)–Fe(1)–N(5)	166.02 (13)	163.81 (10)	156.1 (3)
N(3)–Fe(1)–N(6)	89.85 (13)	89.13 (10)	87.0 (2)
N(4A)–Fe(1)–N(5)	90.93 (13)	90.52 (10)	89.2 (2)
N(4A)–Fe(1)–N(6)	86.57 (13)	85.52 (11)	82.4 (2)
N(5)–Fe(1)–N(6)	78.93 (13)	78.14 (10)	74.3 (2)
Fe(1)–N(1)–C(1)	176.7 (4)	175.8 (3)	173.6 (7)
Fe(1)–N(2)–C(2)	157.9 (4)	157.4 (3)	158.0 (8)

Symmetry code A: $-x + 1, -y, -z + 1$ (complex **1** at 100 K); Symmetry code A: $-x + 1, -y + 2, -z + 1$ (complex **1** at 150 K and 300 K). Octahedral distortion parameter Σ (sum of the deviations from 90° of the 12 cis N–Fe–N angles in the FeN_6 coordination sphere).

Table 2. Selected bond lengths [Å] and angles [°] in the structure of complex **2** at 100 K.

Complex 2			
Fe(1)–N(1)	2.088 (3)	N(1)–Fe(1)–N(6)	89.30 (13)
Fe(1)–N(2)	2.050 (4)	N(2)–Fe(1)–N(3)	109.33 (14)
Fe(1)–N(3)	2.207 (3)	N(2)–Fe(1)–N(4A)	94.25 (14)
Fe(1)–N(4A)	2.246 (3)	N(2)–Fe(1)–N(5)	93.27 (13)
Fe(1)–N(5)	2.229 (3)	N(2)–Fe(1)–N(6)	166.35 (14)
Fe(1)–N(6)	2.178 (4)	N(3)–Fe(1)–N(4A)	73.76 (12)
av. Fe–N(Å)	2.167	N(3)–Fe(1)–N(5)	151.56 (12)
$Fe–Fe_{intramolecular}$(Å)	5.9401	N(3)–Fe(1)–N(6)	84.24 (12)
Σ	88.16	N(4A)–Fe(1)–N(5)	87.94 (12)
N(1)–Fe(1)–N(2)	91.19 (14)	N(4A)–Fe(1)–N(6)	88.11 (13)
N(1)–Fe(1)–N(3)	93.61 (13)	N(5)–Fe(1)–N(6)	73.36 (12)
N(1)–Fe(1)–N(4A)	167.30 (13)	Fe(1)–N(1)–C(1)	168.0 (3)
N(1)–Fe(1)–N(5)	103.22 (13)	Fe(1)–N(2)–C(2)	159.3 (3)

Symmetry code A: $-x + 1, -y + 1, -z + 2$ (complex **2** at 100 K). Octahedral distortion parameter Σ (sum of the deviations from 90° of the 12 cis N–Fe–N angles in the [FeN_6] coordination sphere).

The crystal data acquired at 100 and 150 K show that the unit cell of complex **1** is equivalent to that at 300 K at these temperatures, albeit with smaller unit cell volumes; the cell volume changed from 2254.91 (18) $Å^3$ (at 300 K) to 2162.95 (14) $Å^3$ (at 150 K), which corresponds to a contraction of approximately 4.1% and is indicative of a change in spin state. The cell volume further contracted to 2151.0 (2) $Å^3$ at low temperature (100 K). The Fe–N bond lengths in complex **1** at 300 K range between 2.024 (9) and 2.278 (6) Å, with an average value of 2.161 Å, which indicates that the two Fe^{II} ions in the binuclear molecule are in the high-spin state. The average Fe–N bond length was determined to be 2.010 Å at 100 K, which indicates that the two Fe^{II} ions are in the [LS–LS] state; the average Fe–N bond length was determined to be 2.045 Å at 150 K, which lies between the high- and low-spin values, consistent with an intermediate state. However, no change in space group symmetry was observed, and the structure of the centrally symmetric binuclear molecule was found to be similar to that observed at room temperature. The crystal structures associated with the Fe^{II} coordination environment at various temperatures are similar to those reported in the literature [36–39]. As expected, the intramolecular Fe–Fe distances that correspond to the three temperature points are 5.970, 5.645, and 5.544 Å, respectively, moving from high to low temperature, which means that the intramolecular Fe^{II} distance decreases as the state of the Fe^{II} ion changes from HS to LS.

The lattice solvents (methanol and acetonitrile) in complex **1** are distributed around the {[Fe(abpt-TPE)$(NCS)_2$]$_2$(bpym)} unit at 100 K, with no typical weak $\pi\cdots\pi$ interactions observed due to various degrees of aromatic ring distortion and large distances; however, intramolecular C–H···N hydrogen bonds are observed in the molecular packing arrangement. In addition, three intermolecular hydrogen bonds, namely, C–H···S, O–H···N, and C–H···O (pale purple and red dashed lines), that involve the lattice-solvent molecules are observed. These three intermolecular hydrogen bonds cause complex **1** to form an infinite linear one-dimensional chain (red solid line) along the *b* axis (Figure 4). The corresponding Fe–Fe distance between the shortest dimers in the chain was determined to be 12.294 Å; this distance increased with increasing temperature to 12.325 Å at 150 K and 12.451 Å at 300 K. Identical molecular packing arrangements were observed at both low and room temperatures; however, weaker intermolecular hydrogen bonds were observed at the latter.

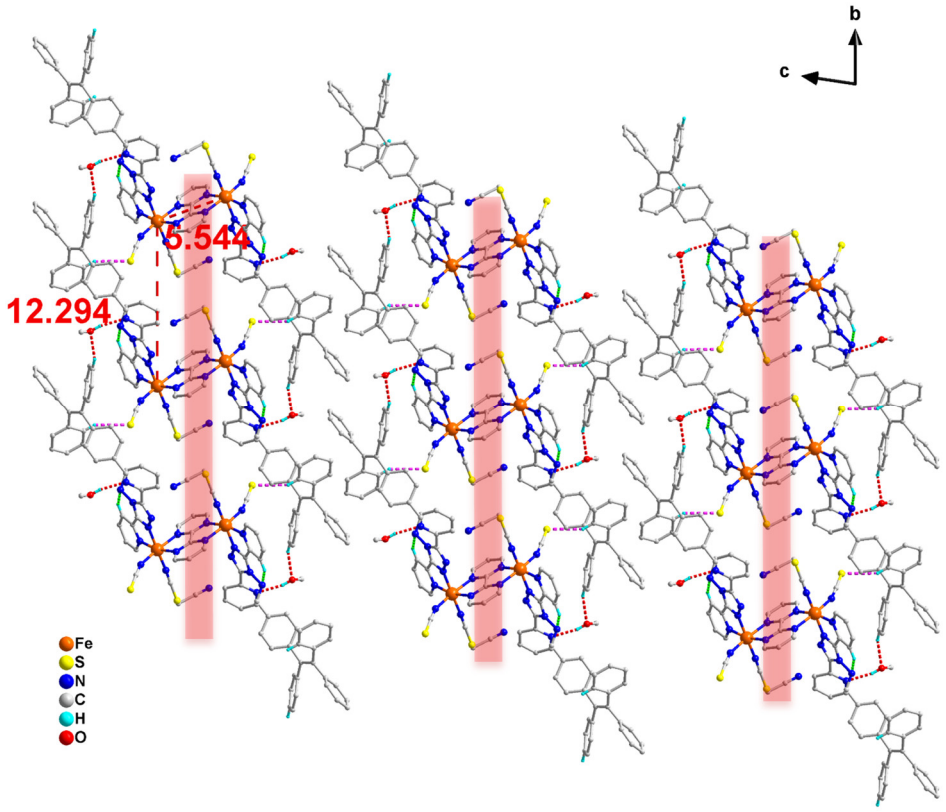

Figure 4. Schematic showing the crystal packing, lattice solvent distribution, and hydrogen bonding of **1** at 100 K. The pale purple and red dashed lines represent intermolecular hydrogen bonds, and the green dashed lines represent intramolecular hydrogen bonds. The numbers in the figure are distances in Å.

The lattice solvent molecules (dichloromethane) are distributed around the {[Fe(abpt-TPE)$(NCS)_2]_2$(bpym)} unit in complex **2** at 100 K, and intramolecular C–H···N (red dashed lines) and C–H···S hydrogen bonds between these solvent molecules and the binuclear molecules (green dashed lines) are observed. Adjacent molecules form a one-dimensional chain through $\pi\cdots\pi$ interactions involving coordination pyridines (red dashed lines) in the *c*-axis direction. Figure 5 shows that two different stacking modes of the one-dimensional chain alternately expand in the *ab* plane (red and green solid lines).

What factors are responsible for the different magnetic behaviors exhibited for complexes **1** and **2**? Complexes **1** and **2** crystallize in different space groups with different lattice solvents, ligand strains, and crystal stacking modes; these differences may cause the octahedral [FeN_6] geometries of **1** and **2** to distort to different degrees [40]. The solvent effects on the SCO behavior are well documented in the literature [41–46]. In general, higher octahedral distortion (Σ) corresponds to stronger distortion and indicates that ligand-field weakening stabilizes the HS state. Complex **1** exhibited Σ values of 51.83, 60.37, and 90.75 at 100, 150, and 300 K, respectively. The data show that Σ increases and the ligand field weakens with increasing temperature, which benefits the HS state. On the other hand, complex **2** was determined to have a Σ value of 87.53 (100 K); this high Σ value indicates that **2** contains stable Fe^{II}_{HS} ions within its [FeN_6] units in the examined temperature range. Different degrees of distortion cause complexes **1** and **2** to exhibit different magnetic behaviors: complex **1** exhibits two-step spin transition behavior during thermal induction, while complex **2** exhibits antiferromagnetism.

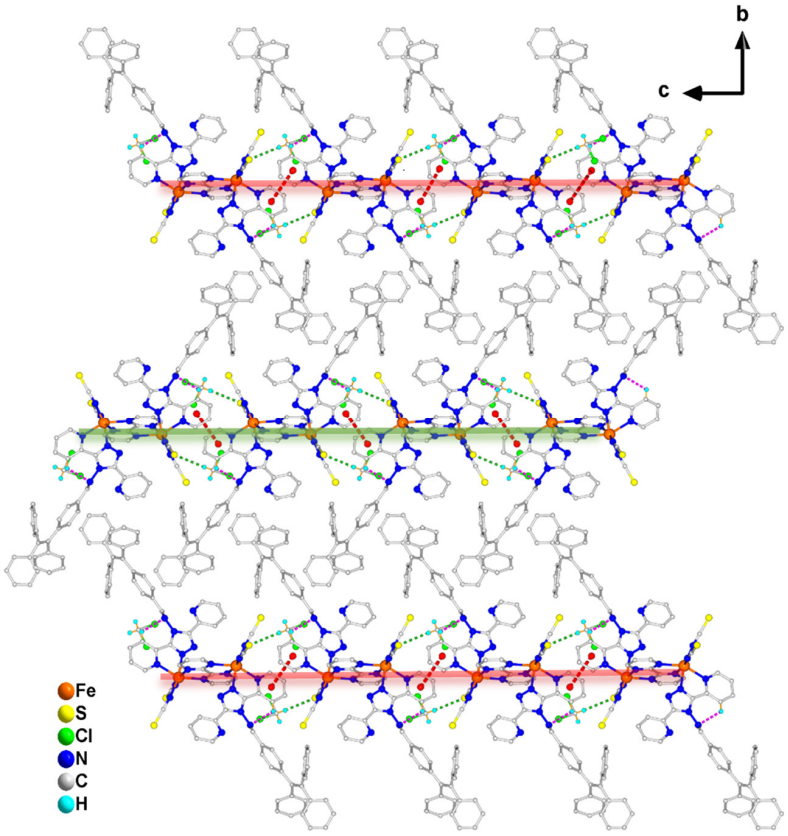

Figure 5. Schematic showing the crystal packing, lattice solvent distribution, hydrogen bonding, and $\pi\cdots\pi$ interactions of **2** at 100 K. The red dashed lines represent $\pi\cdots\pi$ interactions, and the green and pale purple dashed lines represent intramolecular hydrogen bonds.

To explore the relationship between SCO and the fluorescence behavior of compound **1** [47,48], we acquired fluorescence emission spectra of solid compound **1** at various temperatures in heating mode (Figure 6a). **1** exhibited a wide fluorescence emission band (370–700 nm) with an emission wavelength maximum of approximately 479 nm. The maximum fluorescence intensity at 80 K was determined to be approximately three times higher than that recorded at 300 K. The fluorescence emission intensity decreased monotonically as the temperature was gradually increased from 80 to 340 K (Figure 6b), indicative of a process dominated by temperature-controlled thermal quenching. The fluorescence spectra reveal that SCO and fluorescence coexist independently in complex **1**.

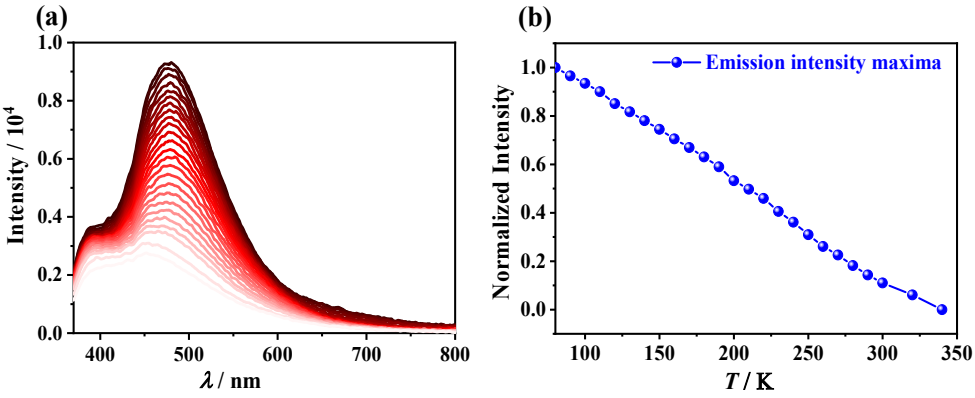

Figure 6. (**a**) Variable-temperature fluorescence emission spectra of **1**; (**b**) Normalized maximum fluorescence emission intensity of **1** as a function of temperature.

3. Experimental Section

3.1. Synthesis

All Fe^{II} complexes were handled in a glove box under argon. Unless otherwise stated, solvents, such as anhydrous ethanol, methanol, and acetonitrile, were purchased through commercial channels. $Fe(py)_4(NCS)_2$ and *N*-(3,5-di(pyridine-2-yl)-4*H*-1,2,4-triazol-4-yl)-1-(4-(1,2,2-triphenylvinyl)phenyl)methanimine (abpt-TPE) were synthesized according to previous literature procedures [26].

3.1.1. {[Fe(abpt-TPE)$(NCS)_2$]$_2$(bpym)}·2MeOH·2MeCN (**1**)

Abpt-TPE (34.8 mg, 0.06 mmol) was dissolved in dichloromethane (8 mL), after which the solution was added to acetonitrile (8 mL). The resulting solution was slowly dropped into a methanol solution (16 mL) containing ascorbic acid (8.8 mg) and $Fe(py)_4(NCS)_2$ (29.2 mg, 0.03 mmol), after which it was stirred at room temperature for 5 min, which resulted in a red solution. Solid 2,2′-bipyrimidine (9.4 mg, 0.06 mmol) was then added, and stirring continued for another 10 min, resulting in a clear dark-red solution. Purple needle-like crystals were obtained after storing the solution in ether vapor for one week. Yield: 46.4% (based on abpt-TPE). Elemental analysis (%) calculated for dried {[Fe(abpt-TPE)$(NCS)_2$]$_2$(bpym)} ($C_{90}H_{62}Fe_2N_{20}S_4$): C, 64.98; H, 3.76; N, 16.84. Found for dried **1**: C, 64.84; H, 3.77; N, 16.70.

3.1.2. {[Fe(abpt-TPE)$(NCS)_2$]$_2$(bpym)}·2CH_2Cl_2 (**2**)

Abpt-TPE (34.8 mg, 0.06 mmol) was dissolved in dichloromethane (8 mL) with stirring, after which it was gradually added to a methanol solution (16 mL) containing ascorbic acid (8.8 mg) and $Fe(py)_4(NCS)_2$ (29.2 mg, 0.03 mmol). The solution was stirred at room temperature for 5 min, after which 2,2′-bipyrimidine (4.8 mg, 0.03 mmol) was added, with stirring continued for 10 min at room temperature. The obtained dark-red solution was placed in ether vapor to afford long block crystals with red–brown aggregates after a few days. Yield: 59.3% (based on abpt-TPE). Elemental analysis (%) calculated for dried {[Fe(abpt-TPE)$(NCS)_2$]$_2$(bpym)} ($C_{90}H_{62}Fe_2N_{20}S_4$): C, 64.98; H, 3.76; N, 16.84. Found for dried **2**: C, 64.65; H, 3.84; N, 16.30.

3.2. Single Crystal X-ray Diffractometry (SCXRD)

SCXRD data for complexes 1 and 2 were acquired on a Rigaku XtalAB PRO MM007 DW diffractometer. The collected diffraction data were integrated and restored using the CrystalAlice PRO program, after which each single-crystal structure was analyzed and refined using Olex2 software. The free disorder in the structure of complex **2** was removed using the squeeze command, and all non-hydrogen atoms were treated anisotropically.

3.3. Powder X-ray Diffractometry (PXRD)

Experimental powder X-ray diffraction data for the two complexes were acquired in the 3–60° range at 5 °C min^{-1} and room temperature using a Rigaku Smart Lab 3 kW X-ray powder diffractometer. The calculated patterns were generated using Mercury software.

3.4. Magnetic Measurements

Variable-temperature susceptibilities were measured using a Quantum Design SQUID MPMS-3 magnetometer at 10–300 K in sweep mode in a 1000 Oe magnetic field at 5 K min^{-1}. The relationship between magnetization (*M*) and field (*H*) for complex **2** was determined at 2 K.

3.5. Fluorescence Spectroscopy

Variable-temperature fluorescence emission spectra of **1** from 80 to 340 K were acquired on an Edinburgh FLS 1000 fluorescence spectrophotometer in heating mode. Each sample was placed in a copper groove substrate and covered with a quartz plate.

3.6. Other Characterization

Elemental analyses were performed using a Vario EL cube analyzer on dried samples after desolvation. Thermogravimetric analysis (TGA) was carried out under argon using a TG–DTA analyzer (Nippon Institute of Physics) heated at 10 °C min^{-1}. Differential scanning calorimetry (DSC) was performed using a TA DSC-25 instrument (New Castle, DE, USA) with 5 K min^{-1} heating and cooling rates.

4. Conclusions

We designed and synthesized two binuclear complexes using abpt-TPE as the terminal ligand and bpym as the bridging ligand. The complexes were systematically characterized by X-ray diffractometry, magnetism measurements, and variable-temperature fluorescence emission spectroscopy. Complex **1** exhibited two-step spin transition behavior with multiple spin states: [LS–LS] ↔ [LS¬–HS] ↔ [HS¬–HS]. In contrast, complex **2** remained in the [HS–HS] state, with antiferromagnetic coupling ($J = -0.47$ cm^{-1}) observed between the two covalently bridged Fe^{II}_{HS} units. According to structural analysis, the two compounds have different lattice solvents, ligand strains, and different crystal stacking modes. The above differences cause the [FeN_6] octahedra of compounds **1** and **2** to have different degrees of distortion, so the binuclear compounds show different magnetic behaviors. Interestingly, variable-temperature fluorescence emission spectroscopy shows that the fluorescence intensity of **1** decreases monotonically with increasing temperature, dominated by the thermal quenching effect affected by temperature. Thus, SCO and fluorescence coexist in complex **1**. This work further highlights the important influence of [FeN_6] octahedral distortion caused by solvents, ligand strain, and crystal packing on the magnetic behavior of a binuclear complex. Moreover, this work contributes to the design and construction of binuclear and multinuclear magnetic complexes.

Supplementary Materials: The following supporting information can be downloaded at https://www.mdpi.com/article/10.3390/magnetochemistry9030069/s1: Figure S1: PXRD for complexes **1** (top) and **2** (bottom) at room temperature; Figure S2: TG curves of complexes **1** (top) and **2** (bottom); Figure S3: Plot of magnetization (*M*) vs. field (*H*) for complex **2**; Figure S4: DSC curves for complex **1** in the heating and cooling modes; Table S1: Selected crystallographic data for complex **1**; Table S2: Selected crystallographic data for complex **2**.

Author Contributions: Conceptualization and investigation, Y.L., Y.G. and Y.-Q.L. analyzed the results and wrote the first draft of the manuscript; writing—review, Y.-Y.W. and J.-H.W. performed the magnetization calculations; supervision, resources, project administration and funding acquisition, J.-W.D., Z.-Y.L. and M.Y. All authors have read and agreed to the published version of the manuscript.

Funding: This research was funded by the National Natural Science Foundation of China (NSFC; 21971124, 22275100).

Institutional Review Board Statement: Not applicable.

Informed Consent Statement: Not applicable.

Data Availability Statement: Data are contained within the article or Supplementary Materials.

Acknowledgments: We especially thank Nankai University for startup funds in support of the talented young researchers.

Conflicts of Interest: The authors declare no conflict of interest.

References

1. Kahn, O.; Martinez, C.J. Spin-Transition Polymers: From Molecular Materials toward Memory Devices. *Science* **1998**, *279*, 44–48. [CrossRef]
2. Bousseksou, A.; Molnár, G.; Salmon, L.; Nicolazzi, W. Molecular spin crossover phenomenon: Recent achievements and prospects. *Chem. Soc. Rev.* **2011**, *40*, 3313–3335. [CrossRef] [PubMed]
3. Shepherd, H.J.; Gural'skiy, I.A.; Quintero, C.M.; Tricard, S.; Salmon, L.; Molnar, G.; Bousseksou, A. Molecular actuators driven by cooperative spin-state switching. *Nat. Commun.* **2013**, *4*, 1–9. [CrossRef] [PubMed]

4. Brooker, S. Spin crossover with thermal hysteresis: Practicalities and lessons learnt. *Chem. Soc. Rev.* **2015**, *44*, 2880–2892. [CrossRef]
5. Kumar, S.K.; Ruben, M. Emerging trends in spin crossover (SCO) based functional materials and devices. *Coord. Chem. Rev.* **2017**, *346*, 176–205. [CrossRef]
6. Wang, M.; Li, Z.Y.; Ishikawa, R.; Yamashita, M. Spin crossover and valence tautomerism conductors. *Coord. Chem. Rev.* **2021**, *435*, 213819. [CrossRef]
7. Hogue, R.W.; Singh, S.; Brooker, S. Spin crossover in discrete polynuclear iron(ii) complexes. *Chem. Soc. Rev.* **2018**, *47*, 7303–7338. [CrossRef]
8. Halcrow, M.A. Structure:function relationships in molecular spin-crossover complexes. *Chem. Soc. Rev.* **2011**, *40*, 4119–4142. [CrossRef]
9. Li, A.M.; Hochdörffer, T.; Wolny, J.A.; Schünemann, V.; Rentschler, E. Abrupt Spin Crossover Behavior in a Linear N1,N2-Triazole Bridged Trinuclear Fe(II) Complex. *Magnetochemistry* **2018**, *4*, 34. [CrossRef]
10. Craig, G.A.; Roubeau, O.; Aromí, G. Spin state switching in 2,6-bis(pyrazol-3-yl)pyridine (3-bpp) based Fe(II) complexes. *Coord. Chem. Rev.* **2014**, *269*, 13–31. [CrossRef]
11. Halcrow, M.A. Iron(II) complexes of 2,6-di(pyrazol-1-yl)pyridines—A versatile system for spin-crossover research. *Coord. Chem. Rev.* **2009**, *253*, 2493–2514. [CrossRef]
12. Boillot, M.L.; Weber, B. Mononuclear ferrous and ferric complexes. *Comptes Rendus Chim.* **2018**, *21*, 1196–1208. [CrossRef]
13. Sciortino, N.F.; Scherl-Gruenwald, K.R.; Chastanet, G.; Halder, G.J.; Chapman, K.W.; Letard, J.F.; Kepert, C.J. Hysteretic three-step spin crossover in a thermo- and photochromic 3D pillared Hofmann-type metal-organic framework. *Angew. Chem. Int. Ed.* **2012**, *124*, 10301–10305. [CrossRef]
14. Bartual-Murgui, C.; Akou, A.; Salmon, L.; Molnar, G.; Thibault, C.; Real, J.A.; Bousseksou, A. Guest effect on nanopatterned spin-crossover thin films. *Small* **2011**, *7*, 3385–3391. [CrossRef] [PubMed]
15. Bao, X.; Shepherd, H.J.; Salmon, L.; Molnar, G.; Tong, M.L.; Bousseksou, A. The effect of an active guest on the spin crossover phenomenon. *Angew. Chem. Int. Ed.* **2013**, *125*, 1236–1240. [CrossRef]
16. Gaspar, A.B.; Muñoz, M.C.; Real, J.A. Dinuclear iron(ii) spin crossover compounds: Singular molecular materials for electronics. *J. Mater. Chem.* **2006**, *16*, 2522–2533. [CrossRef]
17. Sulaiman, A.; Jiang, Y.Z.; Javed, M.K.; Wu, S.Q.; Li, Z.Y.; Bu, X.H. Tuning of spin-crossover behavior in two cyano-bridged mixed-valence $FeIII_2FeII$ trinuclear complexes based on a Tp^R ligand. *Inorg. Chem. Front.* **2022**, *9*, 241–248. [CrossRef]
18. Wang, J.H.; Vignesh, K.R.; Zhao, J.; Li, Z.Y.; Dunbar, K.R. Charge transfer and slow magnetic relaxation in a series of cyano-bridged $FeIII_4MII_2$ (M = Fe^{II}, Co^{II}, Ni^{II}) molecules. *Inorg. Chem. Front.* **2019**, *6*, 493–497. [CrossRef]
19. Klokishner, S.; Ostrovsky, S.; Palii, A.; Tsukerblat, B. Cooperative Spin Transitions Triggered by Phonons in Metal Complexes Coupled to Molecular Vibrations. *Magnetochemistry* **2022**, *8*, 24. [CrossRef]
20. Bousseksou, A.; Molnár, G.; Real, J.A.; Tanaka, K. Spin crossover and photomagnetism in dinuclear iron(II) compounds. *Coord. Chem. Rev.* **2007**, *251*, 1822–1833. [CrossRef]
21. Wu, D.Y.; Sato, O.; Einaga, Y.; Duan, C.Y. A spin-crossover cluster of iron(II) exhibiting a mixed-spin structure and synergy between spin transition and magnetic interaction. *Angew. Chem. Int. Ed.* **2009**, *48*, 1475–1478. [CrossRef] [PubMed]
22. Wang, J.; Dai, J.W.; Li, Z.Y.; Yamashita, M. Strong antiferromagnetic coupling of the cobalt(ii)-semiquinone radical in a dinuclear complex with 2,2′-bipyrimidine ligands. *New J. Chem.* **2020**, *42*, 3963–4776. [CrossRef]
23. Klein, Y.; Sciortino, N.F.; Housecroft, C.E.; Kepert, C.J.; Neville, S.M. Structure and Magnetic Properties of the Spin Crossover Linear Trinuclear Complex $[Fe_3(furtrz)_6(ptol)_2(MeOH)_4]\cdot4(ptol)\cdot4(MeOH)$ (furtrz: Furanylidene-4H-1,2,4-triazol-4-amine ptol: P-tolylsulfonate). *Magnetochemistry* **2016**, *2*, 7. [CrossRef]
24. Furmeyer, F.; Carrella, L.M.; Ksenofontov, V.; Moller, A.; Rentschler, E. Phase Trapping in Multistep Spin Crossover Compound. *Inorg. Chem. Front.* **2020**, *59*, 2843–2852. [CrossRef]
25. Wang, J.H.; Li, Z.Y.; Yamashita, M.; Bu, X.H. Recent progress on cyano-bridged transition-metal-based single-molecule magnets and single-chain magnets. *Coord. Chem. Rev.* **2021**, *428*, 213617. [CrossRef]
26. Li, Y.; Javed, M.K.; Wu, S.Q.; Sulaiman, A.; Wu, Y.Y.; Li, Z.Y.; Sato, O.; Bu, X.H. Aggregation-induced emission meets magnetic bistability: Synergy between spin crossover and fluorescence in iron(ii) complexes. *Chin. Chem. Lett.* **2022**, *34*, 107492. [CrossRef]
27. Yi, C.; Meng, Y.S.; Zhao, L.; Yao, N.T.; Liu, Q.; Wen, W.; Li, R.X.; Zhu, Y.Y.; Oshio, H.; Liu, T. A Smart Molecule Showing Spin Crossover Responsive Aggregation-Induced Emission. *CCS Chem.* **2022**, 1–10. [CrossRef]
28. Leita, B.A.; Moubaraki, B.; Murray, K.S.; Smith, J.P.; Cashion, J.D. Structure and magnetism of a new pyrazolate bridged iron(II) spin crossover complex displaying a single HS-HS to LS-LS transition. *Chem. Commun.* **2003**, *2004*, 156–157. [CrossRef]
29. Moussa, N.O.; Trzop, E.; Mouri, S.; Zein, S.; Molnár, G.; Gaspar, A.B.; Collet, E.; Cointe, M.B.L.; Real, J.A.; Borshch, S.; et al. Wavelength selective light-induced magnetic effects in the binuclear spin crossover compound $\{[Fe(bt)(NCS)_2]_2(bpym)\}$. *Phys. Rev. B* **2007**, *75*, 054101. [CrossRef]
30. Schneider, C.J.; Cashion, J.D.; Chilton, N.F.; Etrillard, C.; Fuentealba, M.; Howard, J.A.K.; Létard, J.F.; Milsmann, C.; Moubaraki, B.; Sparkes, H.A.; et al. Spin Crossover in a 3,5-Bis(2-pyridyl)-1,2,4-triazolate-Bridged Dinuclear Iron(II) Complex $[\{Fe(NCBH_3)(py)\}_2(\mu\text{-}L^1)_2]$—Powder versus Single Crystal Study. *Eur. J. Inorg. Chem.* **2012**, *2013*, 850–864. [CrossRef]
31. Albores, P.; Rentschler, E. cis-2,2′-Bipyrimidine-bridged polynuclear complex: A stairway-like mixed-valent $\{Fe_4\}$ cluster. *Inorg. Chem. Front.* **2010**, *49*, 8953–8961. [CrossRef] [PubMed]

32. Zein, S.; Borshch, S.A. Energetics of Binuclear Spin Transition Complexes. *J. Am. Chem. Soc.* **2005**, *127*, 16197–16201. [CrossRef] [PubMed]
33. Létard, J.F.; Real, J.A.; Moliner, N.; Gaspar, A.B.; Capes, L.; Cador, O.; Kahn, O. Light Induced Excited Pair Spin State in an Iron(II) Binuclear Spin-Crossover Compound. *J. Am. Chem. Soc.* **1999**, *121*, 10630–10631. [CrossRef]
34. Batten, S.R.; Bjernemose, J.; Jensen, P.; Leita, B.A.; Murray, K.S.; Moubaraki, B.; Smith, J.P.; Toftlund, H. Designing dinuclear iron(II) spin crossover complexes. Structure and magnetism of dinitrile-, dicyanamido-, tricyanomethanide-, bipyrimidine- and tetrazine-bridged compounds. *Dalton Trans.* **2004**, *20*, 3370–3375. [CrossRef]
35. Venkataramani, S.; Jana, U.; Dommaschk, M.; Sönnichsen, F.D.; Tuczek, F.; Herges, R. Magnetic Bistability of Molecules in Homogeneous Solution at Room Temperature. *Science* **2011**, *331*, 445–448. [CrossRef]
36. Matouzenko, G.S.; Jeanneau, E.; Verat, A.Y.; Bousseksou, A. Spin crossover and polymorphism in a family of 1,2-bis(4-pyridyl)ethene-bridged binuclear iron(II) complexes. A key role of structural distortions. *Dalton Trans.* **2011**, *40*, 9608–9618. [CrossRef]
37. Trzop, E.; Cointe, B.L.M.; Cailleau, H.; Toupet, L.; Molnar, G.; Bousseksou, A.; Gaspar, A.B.; Real, J.A.; Collet, E. Structural investigation of the photoinduced spin conversion in the dinuclear compound {[Fe(bt)$(NCS)_2$]$_2$(bpym)}: Toward controlled multi-stepped molecular switches. *J. Appl. Crystallogr.* **2007**, *40*, 158–164. [CrossRef]
38. De Gaetano, Y.; Jeanneau, E.; Verat, A.Y.; Rechignat, L.; Bousseksou, A.; Matouzenko, G.S. Ligand-Induced Distortions and Magneto-Structural Correlations in a Family of Dinuclear Spin Crossover Compounds with Bipyridyl-Like Bridging Ligands. *Eur. J. Inorg. Chem.* **2013**, *2013*, 1015–1023. [CrossRef]
39. Verat, A.Y.; Ould-Moussa, N.; Jeanneau, E.; Le Guennic, B.; Bousseksou, A.; Borshch, S.A.; Matouzenko, G.S. Ligand strain and the nature of spin crossover in binuclear complexes: Two-step spin crossover in a 4,4′-bipyridine-bridged iron(II) complex [{Fe(dpia)$(NCS)_2$}$_2$(4,4′-bpy)] (dpia = di(2-picolyl)amine; 4,4′-bpy = 4,4′-bipyridine). *Chem. Eur. J.* **2009**, *15*, 10070–10082. [CrossRef]
40. Ding, Z.Y.; Meng, Y.S.; Xiao, Y.; Zhang, Y.Q.; Zhu, Y.Y.; Gao, S. Probing the influence of molecular symmetry on the magnetic anisotropy of octahedral cobalt(ii) complexes. *Inorg. Chem. Front.* **2017**, *4*, 1909–1916. [CrossRef]
41. Amoore, J.J.M.; Neville, S.M.; Moubaraki, B.; Iremonger, S.S.; Murray, K.S.; Letard, J.F.; Kepert, C.J. Thermal- and Light-induced spin crossover in a guest-dependent dinuclear iron(II) system. *Chem.-Eur. J.* **2010**, *16*, 1973–1982. [CrossRef] [PubMed]
42. Ortega-Villar, N.; Thompson, A.L.; Munoz, M.C.; Ugalde-Saldivar, V.M.; Goeta, A.E.; Moreno-Esparza, R.; Real, J.A. Solid- and solution-state studies of the novel mu-dicyanamide-bridged dinuclear spin-crossover system [(Fe(bztpen)]$_2$[mu-$N(CN)_2$]$(PF_6)_3$ n H_2O. *Chem.-Eur. J.* **2005**, *11*, 5721–5734. [CrossRef] [PubMed]
43. Real, J.A.; Gaspar, A.B.; Munoz, M.C. Thermal, pressure and light switchable spin-crossover materials. *Dalton Trans.* **2005**, 2062–2079. [CrossRef] [PubMed]
44. Real, J.A.; Munoz, M.C.; Andres, E.; Garnier, T.; Gallois, B. Spin-Crossover Behavior in the Fe(tap)$_2$$(NCS)_2$▪n$CH_3CN$ System (tap=1,4,5,8-Tetraazaphenanthrene; n = 1,1/2). Craystal Structures and Magnetic Properties of Both Solvates. *Inorg. Chem.* **1994**, *33*, 3587–3594. [CrossRef]
45. Cecconi, F.; Vaira, M.D.; Modollini, S.; Orlandini, A.; Sacconi, L. Singlet ⇋ Quintet Spin Transitions of Iron(II) Complexes with a P_4Cl_2 Donor Set. X-ray Structures of the Compound $FeCl_2$ (Ph_2PCH = $CHPPh_2$)$_2$ and of Its Acetone Solvate at 130 and 295K. *Inorg. Chem.* **1981**, *20*, 3423–3430. [CrossRef]
46. Greenaway, A.M.; O'Connor, C.J.; Schrock, A.; Sinn, E. High- and Low-Spin Interconversion in a Series of (α-Picolylamine)iron(II) Complexes. *Inorg. Chem.* **1979**, *18*, 2692–2695. [CrossRef]
47. Javed, M.K.; Sulaiman, A.; Yamashita, M.; Li, Z.Y. Shedding light on bifunctional luminescent spin crossover materials. *Coord. Chem. Rev.* **2022**, *467*, 214625. [CrossRef]
48. Wang, C.F.; Wu, J.H.; Li, Q.X. Synchronously tuning the spin-crossover and fluorescence properties of a two-dimensional Fe(II) coordination polymer by solvent guests. *Inorg. Chem. Front.* **2022**, *9*, 3251–3258. [CrossRef]